Available online at www.sciencedirect.com

SciVerse ScienceDirect

Ceramics International 38 (2012) 5957–5966

CERAMICS INTERNATIONAL

www.elsevier.com/locate/ceramint

Influence of addition of copper cadmium ferrite on the dielectric and electrical behavior of $BaSrTiO_3$ ceramics

Kavita Verma, Seema Sharma *

Ferroelectric Research Laboratory, Department of Physics, AN College, Patna 800013, India

Received 23 December 2011; received in revised form 15 April 2012; accepted 15 April 2012
Available online 23 April 2012

Abstract

Polycrystalline composites of $(1-x)$ $(Ba_{0.7}Sr_{0.3}TiO_3)$–$x(Cu_{0.5}Cd_{0.5}Fe_2O_4)$ ($x = 0.15, 0.30, 0.45$) were prepared by a modified wet chemical method. X-ray diffraction studies at room temperature confirmed the formation of polycrystalline composite with perovskite–spinel structure. Scanning electron micrographs also suggest polycrystalline microstructure with the grains of unequal size distributed throughout the pellet samples. Dielectric studies of the composites reveal that the effect of ferrite in the composites is to shift the ferroelectric–non-ferroelectric phase transition to higher temperature side. Complex impedance spectroscopy analysis indicated negative temperature coefficient of resistance behavior identical to semiconductors. The activation energy calculated from the temperature dependence of conductivity pattern shows that the conduction process can occur due to the hopping of electrons between Fe^{3+} and Fe^{2+}, leading to the contribution of both single and doubly-ionized oxygen vacancies.

Keywords: D. Perovskites; X-ray diffraction; Complex impedance spectroscopy; Negative temperature coefficient of resistance

1. Introduction

With the rapid development of portable electronic products and wireless technology, many electronic devices have evolved into collections of highly integrated systems for multiple functionality, faster operating speed, higher reliability, and reduced sizes. This demands the multifunctional integrated components, serving as both inductor and capacitor. As a result, low temperature co-fired ceramics (LTCC) with integrated capacitive ferroelectrics and inductive ferrites has been regarded as a feasible solution through complex circuit designs. However, in the multilayer LTCC structure consisting of ferroelectrics and ferrites layers, there are always many undesirable defects, such as cracks, pores and cambers, owing to the co-firing mismatch between different material layers, which will damage the property and reliability of end products [1]. A single material with both inductance and capacitance is desired for true integration in one element. For example, if the materials with both high permeability and permittivity are used in the anti electromagnetic interference filters, the size of components can be dramatically minimized compared to that of conventional filters composed of discrete inductors and capacitors. Because few phase material in nature can meet such needs [2], the development of ferroelectric–ferromagnetic composite ceramics is greatly motivated.

Recently, electronic composite materials have attracted many researchers and led to an improvement in the piezoelectric, piezomagnetic and mechanical properties, which are applicable for a particular application [3]. The electroceramic composite materials synthesized from two different phases account for the sum, combination and product properties [4]. In such composite materials, electromagnetic coupling occurs and accounts for an excellent magnetoelectric effect [5–7]. They are also significant for the fundamental research on novel coupling properties such as electro-optic, electro-magnetic and other couplings [8] and have potential applications in electromagnetic interference filters, capacitors, transducers and integral chip inductors. Ferrites and ferroelectric materials are used in a large family of microwave and millimeter wave devices. Many material systems, such as $BaTiO_3$/NiCuZn ferrite, $BaTiO_3$/MgCuZn

* Corresponding author.
E-mail address: seema_sharma26@yahoo.com (S. Sharma).

0272-8842/$36.00
http://dx.doi.org/10.1016/j.ceramint.2012.04.048

ferrite, $Pb(Mg_{1/3}Nb_{2/3})O_3$–$Pb(Zn_{1/3}Nb_{2/3})O_3$–$PbTiO_3$/NiCuZn ferrite and $Bi_2(Zn_{1/3}Nb_{2/3})_2O_7$/NiCuZn ferrite, were investigated and found to exhibit fine dielectric and magnetic properties.

Ferrite devices typically have high figures of merit, large bandwidths, low insertion loss, and frequency agility [9]. Current ferrite components, however, present two critical problems for advanced system applications: large size and high cost. Ferroelectric components, on the other hand, provide solutions both in size and cost [10,11]. Size reduction arises from the large relative dielectric constants. These components are also tunable with the application of a modest voltage. Since the tunability is not as good as for ferrites, the voltage tenability and the low cost are advantageous for many applications. It is likely that ferrite–ferroelectric composites could be used to produce small, low cost, and highly tunable elements for microwave applications. Previous works on multifunctional ferrite–ferroelectric composite materials have emphasized static magnetization properties and complex permeability and permittivity [12–15]. $Cu_{0.5}Cd_{0.5}Fe_2O_4$ (CCF) has been in this was selected as magnetic material because it has high resistance, high magnetostriction coefficient, high Curie temperature and low dielectric permittivity and $Ba_{0.7}Sr_{0.3}TiO_3$ (BST) as a ferroelectric because it has high dielectric constant, high piezoelectric coefficient, high tunability and low dielectric loss. The objective of this work is to prepare a series of ferrite–ferroelectric composite materials with a systematic variation in the ferrite loading and to examine the temperature dependence of dielectric constant (ε') and dielectric loss, ac conductivity; and impedance spectroscopic studies.

2. Impedance formalism

The electrical properties of the materials are investigated by a complex impedance spectroscopy (CIS) technique. This technique has a special significance in the analysis of electrical properties of a material because it enables us to examine the correlation of properties (viz. conductivity, dielectric behavior, relaxation characteristics, etc.) with microstructures (i.e. bulk material and grain boundary contributions, etc.) [16]. Further, it is an elegant non-destructive technique that separates the barrier properties attributing to grains (bulk) from grain boundaries, where each of them has different relaxation time. As a result, a separate semicircle in the complex impedance spectrum is formed.

As it is well established that impedance spectroscopy is an effective method to study (a) properties of the intragranular and interfacial regions and their interrelations, (b) their temperature and frequency dependent phenomena in order to separate the individual contributions from the total impedance and (c) their interfaces with electronically conducting electrodes [17–19,16,20], each impedance parameter can be used to highlight a particular aspect of the response of a sample. More interestingly, the impedance measurements enable us to eliminate the error, if any, due to stray frequency effects. The frequency dependence of various impedance parameters of a material can be described via the complex permittivity (ε^*), complex impedance (Z^*), complex admittance (Y^*), complex electric modulus (M^*) and dielectric loss or dissipation factor ($\tan\delta$) [18]. They are in turn related to each other as follows:

$\varepsilon^* = \varepsilon' - \varepsilon''$, where $\varepsilon' = (-Z'')/\omega C_0(Z'^2 + Z''^2)$ and $\varepsilon'' = Z'/\omega C_0(Z'^2 + Z''^2)$

$M^* = M' + jM'' = (1/\varepsilon^*) = j\omega\varepsilon_0 Z^*$; $Z^* = Z' - jZ'' = (1/jC_0\varepsilon^*\omega)$; $Y^* = Y' + jY'' = j\omega C_0$ and $\tan\delta = (\varepsilon''/\varepsilon') = (M''/M') = (Z''/Z') = (Y'/Y'')$ ($\omega = 2\pi f$ is the angular frequency, $'$ and $''$ mark the real and imaginary part of complex parameters (ε^*, Z^*, M^* and Y^*), C_0 is the geometrical capacitance, $j = \sqrt{-1}$. These relations offer a wide scope for a graphical representation of various impedance parameters under different experimental conditions (i.e. temperature, frequency, etc.). The use of function Z^* and Y^* is particularly appropriate for the resistive and/or conductive analysis where the long-range conduction dominates, where as the ε^* and M^* functions are suitable when localized relaxation dominates. So the plotting of a.c. data in terms of impedance, electric modulus and dielectric permittivity simultaneously gives a complete assignment of all the physical processes taking place in the material [21].

3. Experimental procedures

3.1. Preparation of the composites

Piezoelectric phase, BST powder as reported by us [22] was synthesized by sol gel method using barium acetate, strontium acetate, and titanium (IV) isopropoxide as precursors. The magnetic phase, CCF was prepared by citrate precursor method as reported by us [23]. Then, both the calcined powders (1 − x) BST–x CCF with $x = 0$, 0.15, 0.30, 0.45 and 1.00 were mixed together and ball milled for 48 h in acetone medium. The powder composites were uniaxially pressed into cylindrical pellets of diameter ∼10 mm and thickness ∼1 mm using a hydraulic press at a pressure of 8 MPa and sintered at 850°C for 2 h.

3.2. Structural characterization

The crystal structures were examined by an X-ray diffraction (XRD) technique using a Philips Analytical, X'pert-MPD, employing CuKα radiation under the conditions 50 kV and 40 mA. The samples were scanned at an interval of 0.038°/min for 2θ in the range 10°–70°. The identification of the peaks was carried out using the Topas23 refinement program. Microstructural examination of the fractured surface of the ceramics was carried out by scanning electron microscopy (SEM) using a JEOL 6300 scanning electron microscope.

3.3. Electrical characterization

For dielectric measurements, the disk-shaped samples were ground on SiC paper to reduce the thickness to less than 1 mm and coated with silver paste. Dielectric constant, loss tangent and impedance were determined by PSM1735 Impedance Analyzer at frequencies of 1 kHz–10 MHz; samples were

heated from room temperature to 500 °C in a Carbolite (MTF9/15/130) tube furnace.

4. Results and discussion

4.1. Phase identification

The typical X-ray diffraction pattern of a composite containing $(x-1)$ BST–xCCF with $x = 0.0.15$, 0.30, 0.45, 1.00 is shown in Fig. 1(a and b). It can be seen that the two phases, i.e. the ferroelectric and ferrite, are present in the composites. The lattice parameters of the constituent phases were calculated and are given in Table 1. The ferrite phase has a cubic spinel structure and the ferroelectric has a tetragonal perovskite structure. The lattice parameters of the constituent phases are almost the same in all the composites. This indicates that the structure remains the same even if the composition of the composites is varied. All the peaks of the composites are identified. This confirms the successful preparation of two phase composite materials. It is found that the intensity of the ferrite peaks goes on increasing with its content in the composites. Fig. 2(a–e) shows SEM micrographs of present system. It is noted that the average grain diameter increases with decreasing BST concentration and increasing CCF concentration.

4.2. Dielectric properties

Fig. 3a illustrates the temperature dependent dielectric response recorded at 10 kHz for all the samples. The pure ferroelectric phase (BST) shows the phase transition from the ferroelectric to the paraelectric state at 35 °C (T_c) [22]. As the content of the ferroelectric phase decreases, the dielectric constant decreases and the transition temperature shifts towards the higher temperature side. This phenomenon is reported earlier for different composites [24].

Table 1
Variation of electrical parameters (bulk and grain boundary) as a function of composition (x) at 400 °C.

x	R_b (kΩ)	C_b (pF)	R_{gb} (kΩ)	C_{gb} (pF)	E_a (eV)
0.15	1.02	6.754	–	–	0.82
0.30	1.88	7.930	1.161	8.756	1.02
0.45	2.52	8.745	1.956	12.336	1.07

The decrease in the dielectric constant with ferrite is observed due to the Verwey type of electron exchange polarization in the ferrite phase. The electron hopping between Cu^{2+}/Cu^{1+}, Cd^{2+}/Cd^{3+}, and Fe^{2+}/Fe^{3+} causes local displacements in the direction of the applied electric field and influences the dielectric polarization in ferrites. The transition of these composites is ascribed to the ferromagnetic to the paramagnetic phase transition rather than the ferroelectric to the paraelectric phase transition, because the transition temperature of the composites is nearly equal to that of the ferrite phase. The constant values of the dielectric constant at lower temperatures (<100 °C) may be attributed to the fact that over this range of temperature there is not much effect on the overall microstructure of the composite. The large increase in the dielectric constant near T_c is observed due to the temperature dependence of domain wall motion. At room temperature it is difficult for the domain walls to move and hence the dielectric response due to extrinsic contribution is small. At higher temperatures ($>T_c$), domains disappear after phase transition so that the dielectric response is small also. Near transition temperature the thermal energy is comparable to the potential barrier for domain movement and hence the domain wall motion becomes very active. Fig. 3b shows the variation of the dielectric loss angle tanδ as a function of temperature at different frequencies. Just as the dielectric constant curves,

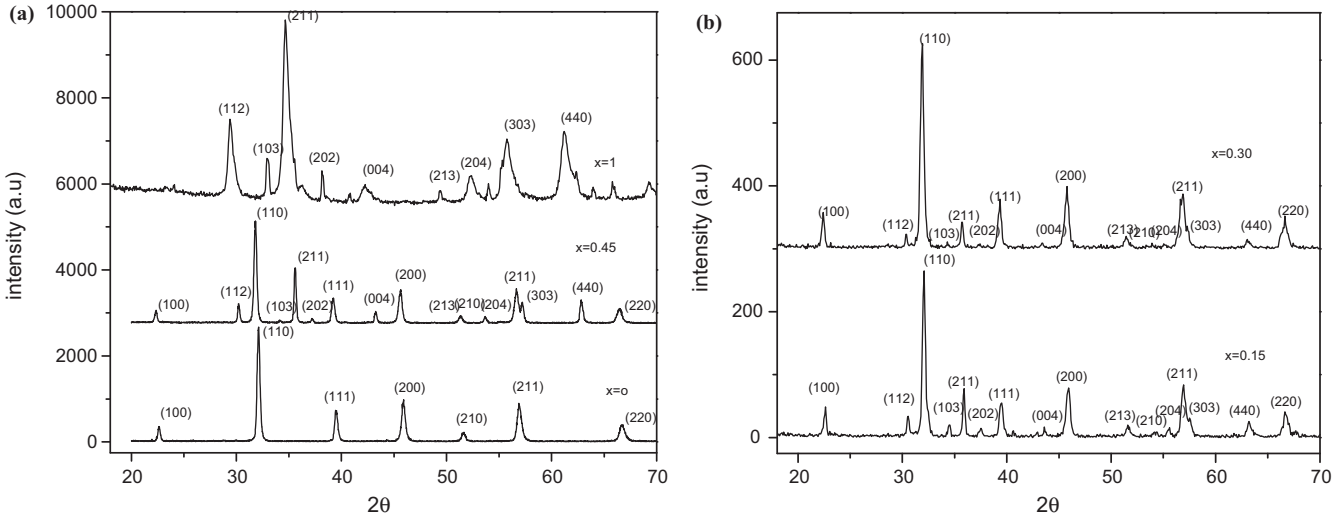

Fig. 1. Room temperature XRD of BST–CCF composites with (a) $x = 0$, 0.45, 1.00, (b) $x = 0.15$, 0.30 sintered at 850 °C.

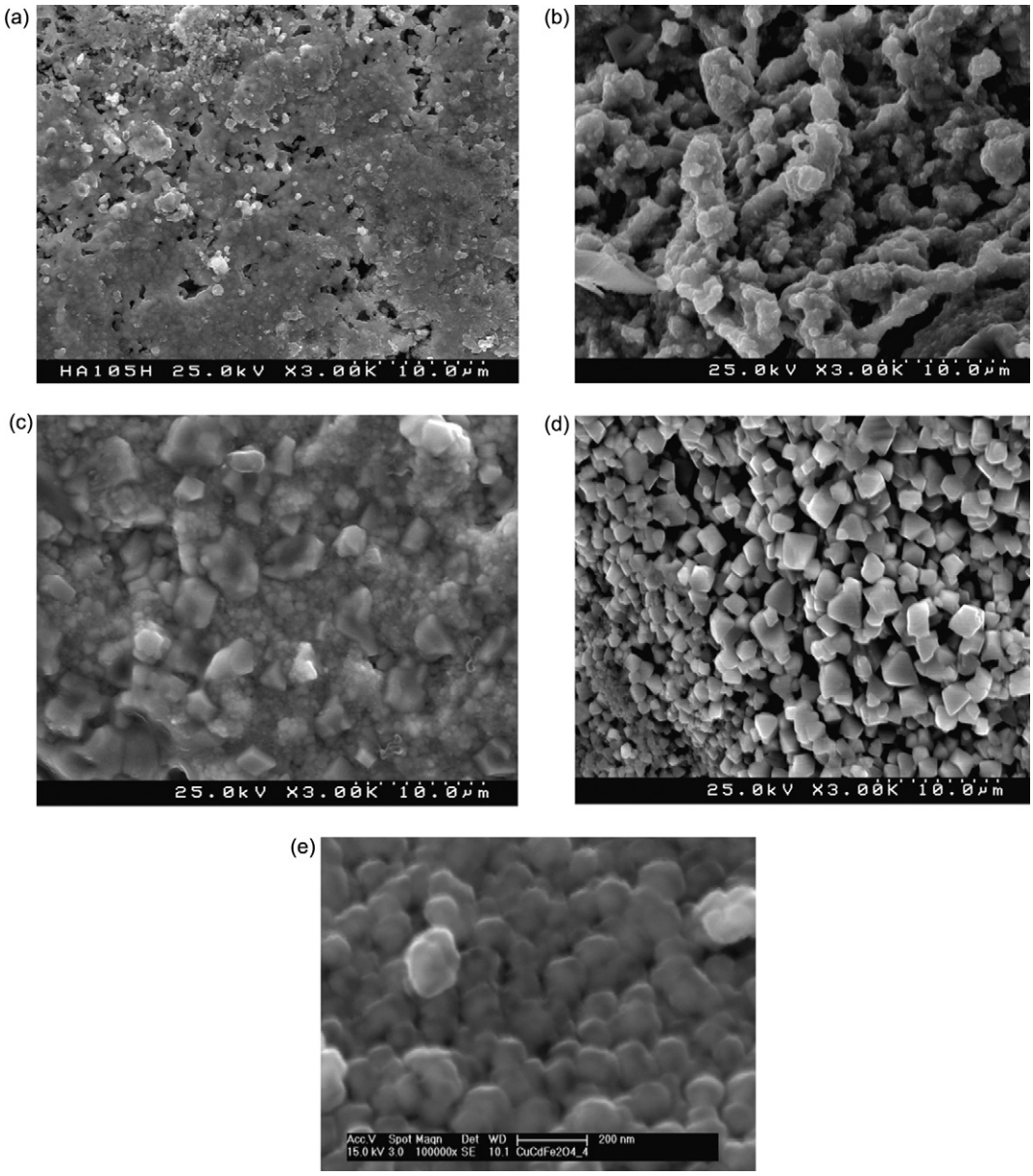

Fig. 2. (a–e) SEM micrographs of BST–CCF composites with $x = 0.0.15, 0.30, 0.45, 1.00$.

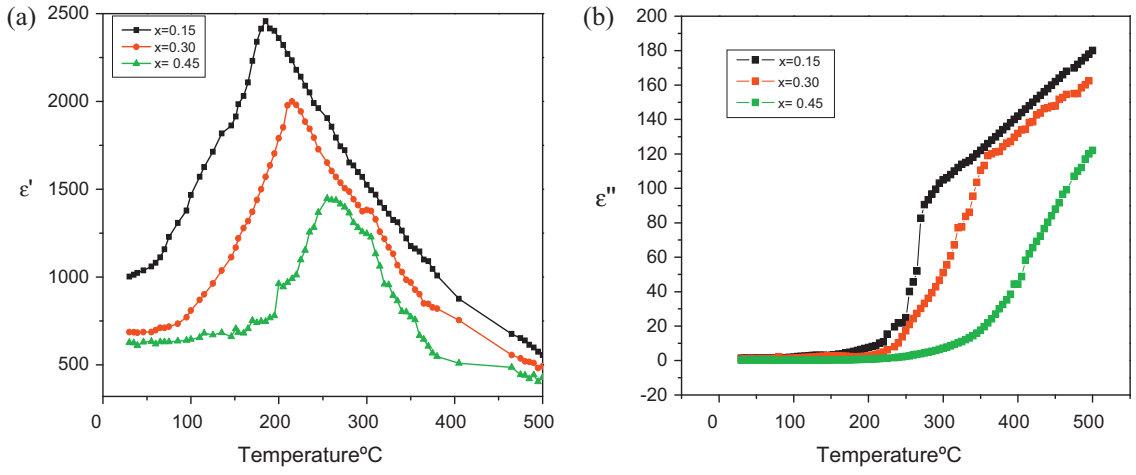

Fig. 3. Temperature variation of (a) ε', (b) ε'' of BST–CCF composites with $x = 0.15, 0.30, 0.45$ at different frequency.

the loss curves also show an increase with temperature and can be explained on lines similar to those advanced for explaining dielectric constant. These curves can be understood on the basis of the Debye equation for loss [25].

$$\tan\delta = \frac{\varepsilon'}{\varepsilon''} = \frac{(\varepsilon_s - \varepsilon_\infty)\omega\tau}{\varepsilon_s - \varepsilon_\infty\omega^2\tau^2}$$

According to this equation, tanδ would increase with decrease in relaxation time for a given frequency. Therefore as the relaxation time decreases with increase in temperature, tanδ increases. The rapid rise in the tanδ curve at higher temperature is attributed to the conduction losses, which increases with temperature due to increased conduction. It is observed that tanδ increases with increase in temperature indicating semiconductor behavior in composites.

The complex impedance of the electrode/ceramic/electrode capacitor can be demonstrated as the sum of the single *R–C* circuit with parallel combination, Fig. 4a(a–c) shows the Z' vs Z'' plot of BST–CCF measured at different temperatures. The effect of temperature on impedance behavior becomes more prominent at higher temperature. The impedance spectrum is characterized by the appearance of semicircular arcs, whose pattern of evolution changes with rise in temperature. The number of semicircular arcs and the extent of their intercept on the real axis provide information regarding the electrical behavior of the compound. A parallel resistance, capacitance circuit corresponding equivalently to the individual component of the materials, i.e. bulk and grain boundary represents a semicircle. The increase in temperature leads to the increase in the semicircular nature of the arcs, with a shift in the center of the arc towards the origin of

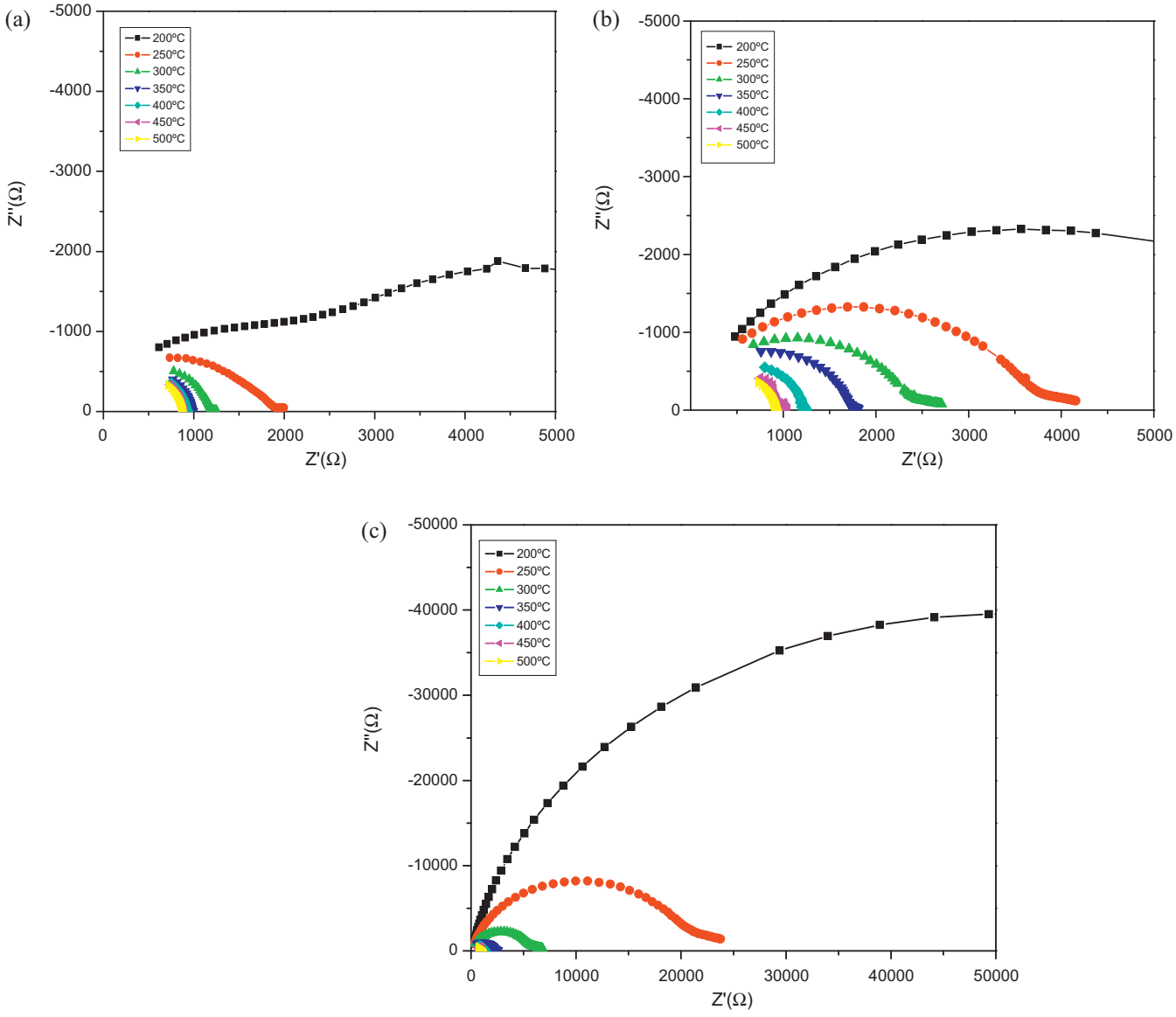

Fig. 4a. Variation of real and imaginary part of impedance of BST–CCF composites with $x = 0.15, 0.30, 0.45$ at different temperature.

the complex plane plot Fig. 4a(a–c). The presence of a single semicircular arc indicates that the electrical process contribution is from a bulk material grain interior, which can be modeled as an equivalent circuit comprising of a parallel combination of bulk resistance and bulk capacitance. Appearance of another semicircular arc near 250 °C indicates the beginning of the intergranular activities grain boundary effect within the sample with definite contributions from both bulk grain interior and grain boundary effects. The values of the circuit elements obviously depend on the volume fraction of the individual components, i.e. grain and grain boundary effect, which is related to the microstructure of the compound. In order to establish a connection between the microstructure and the electrical properties, several microstructural models are discussed in the literature, which usually fall into two types: the layer models and the effective medium models. In ceramics, which are used because of their high dielectric permittivity, grain boundaries are often electronically active due to depletion effects and act as barriers to the cross transport of the charge carriers. The electrical phenomena can be expressed in terms of a bricklayer model, where the conduction through the grain and grain boundaries dominates [26] with equivalent electrical circuit having different values of capacitance and resistance (Table 1). The resistance value was evaluated from the impedance spectrum using the equivalent circuit (EQUIV-CRT) software program [27] whereas the capacitance can be calculated using the following relations:

$$(2\pi f)(R_b C_b) = 1,$$

$$C_b = \frac{1}{(2\pi f)(R_b)}$$

where $\omega = 2\pi f$ is the angular frequency, R_b the bulk resistance, C_b is the bulk capacitance.

This relation is also valid for grain boundary effects. The absence of a third semicircle suggests that the contribution of the electrode–material interface to impedance is negligible. The analysis of the curves shows that the semicircle exhibits some depression degree instead of a semicircle centered on the abscissa axis. This decentralization or non-Debye-type relaxation obeys the Cole–Cole formalism [20] where the depressed semicircle represents typically a phenomenon with a spread of relaxation time. The non-ideal behavior is correlated to several factors such as grain size distribution, grain orientation and grain boundaries. The affect of temperature on impedance behavior of the sample becomes clearly visible from the pattern of the above plot. As the temperature increases the intercept of the prominent semicircles on the Z-axis shifts towards lower values of Z', which indicates the reduction of grain (grain boundary, interface resistance if exist) resistance. The decrease of bulk resistance of the material is more prominent at temperatures around 400–500 °C. This may be due to ionic conduction which is more prominent at higher temperature. An equivalent circuit is being used to provide a complete picture of the system and establish the structural property relationship of the materials. Comparison of complex impedance plots with fitted data using commercially available software ZSimp WIN Version 2 has been given in Fig. 4b. To model the non-Debye

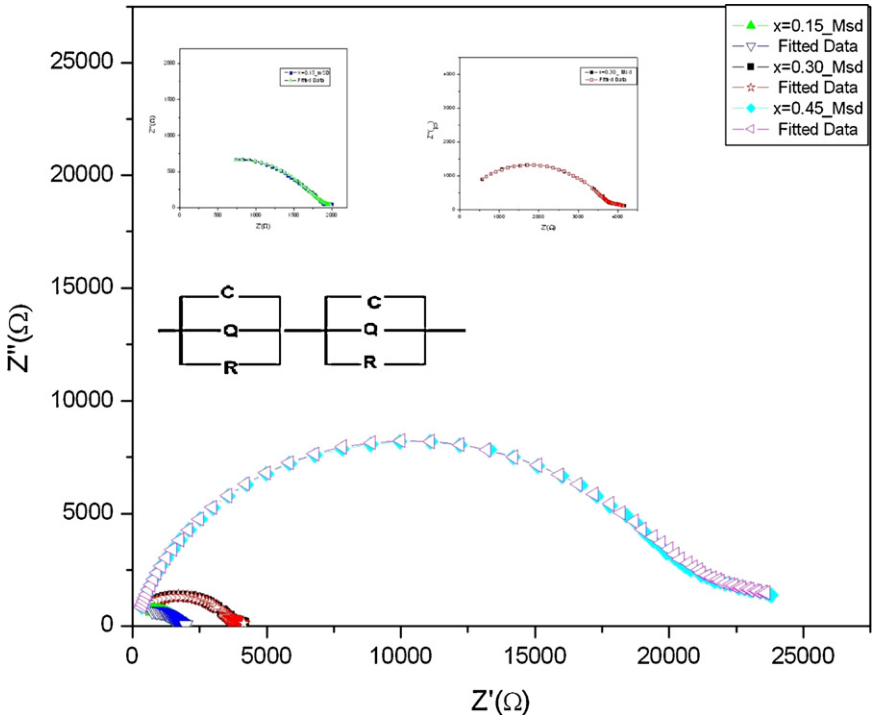

Fig. 4b. Variation of real and imaginary part of impedance of BST–CCF composites (measured and calculated) with $x = 0.45$ at 250 °C.

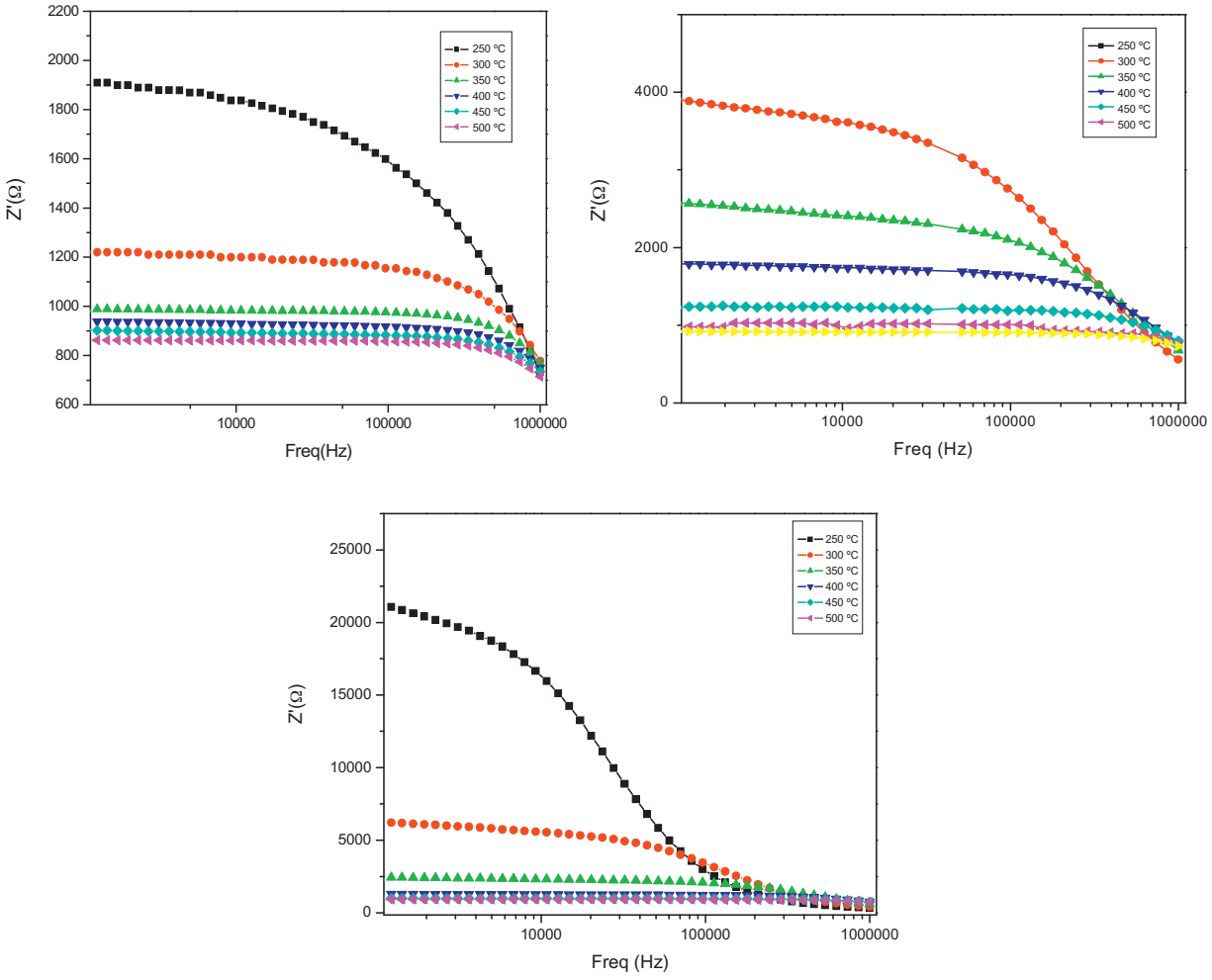

Fig. 5. Frequency variation of real part of impedance of BST–CCF composites with $x = 0.15, 0.30, 0.45$ at different temperature.

response, constant phase element (CPE) is used in addition to resistors and capacitors. The electric and dielectric properties of the composites are well represented by three parallel elements (CQR–CQR, where C is the capacitor, Q the lossy capacitance and R is the resistance) in series.

Fig. 5(a–c) shows the variation of real part of impedance (Z') as a function of frequency (10^4–10^6 Hz) at different temperatures and compositions. The pattern shows a sigmoidal variation as a function of frequency in the low frequency region followed by a saturation region in the high frequency region. This suggests the presence of mixed nature of polarization behavior in the material. The pattern also shows a very steep Z' dispersion in the low frequency region of the spectrum followed by a plateau region in the high frequency region. The extent of steepness in the low frequency region is observed to have a very strong dependence of Z' on the composition of CCF irrespective of temperature. A decreasing trend of Z' with rise in temperature suggests the presence of negative temperature coefficient of resistance (NTCR) in the material in the low frequency region but tends to merge in the high frequency region at almost all temperatures. These results indicate a possibility of increase in a.c. conductivity with rise in temperature in the high frequency region (possibly) due to the release of space charge, and lowering in the barrier properties of the material.

Fig. 6(a–c) exhibits frequency and temperature dependence of imaginary part of impedance (Z'') for BST–CCF composites. In low temperature/frequency range, Z'' has very high value for all the compositions which decreases with rise in frequency and attains low values. This is an interesting (unusual) trend in the variation of Z'' with frequency/temperature for BST–CCF composite. The appearance and nature of peaks at a characteristic angular frequency $\omega_{max}(=2\pi f_{max})$ provide information on the type and strength of the dielectric relaxation phenomenon occuring in the material. The nature of pattern suggests the presence of weak dielectrical relaxation. The effect of CCF substitution on the electrical behavior of the sample can clearly be seen with the appearance of peaks in the impedance spectrum for $x = 0.30$ and 0.45 respectively. At low temperatures, the spectrum shows a monotonous decrease having dispersive nature of pattern in the low frequency region followed by a plateau at the higher frequencies. This observation clearly suggests the presence of electronic, dipolar and space charge

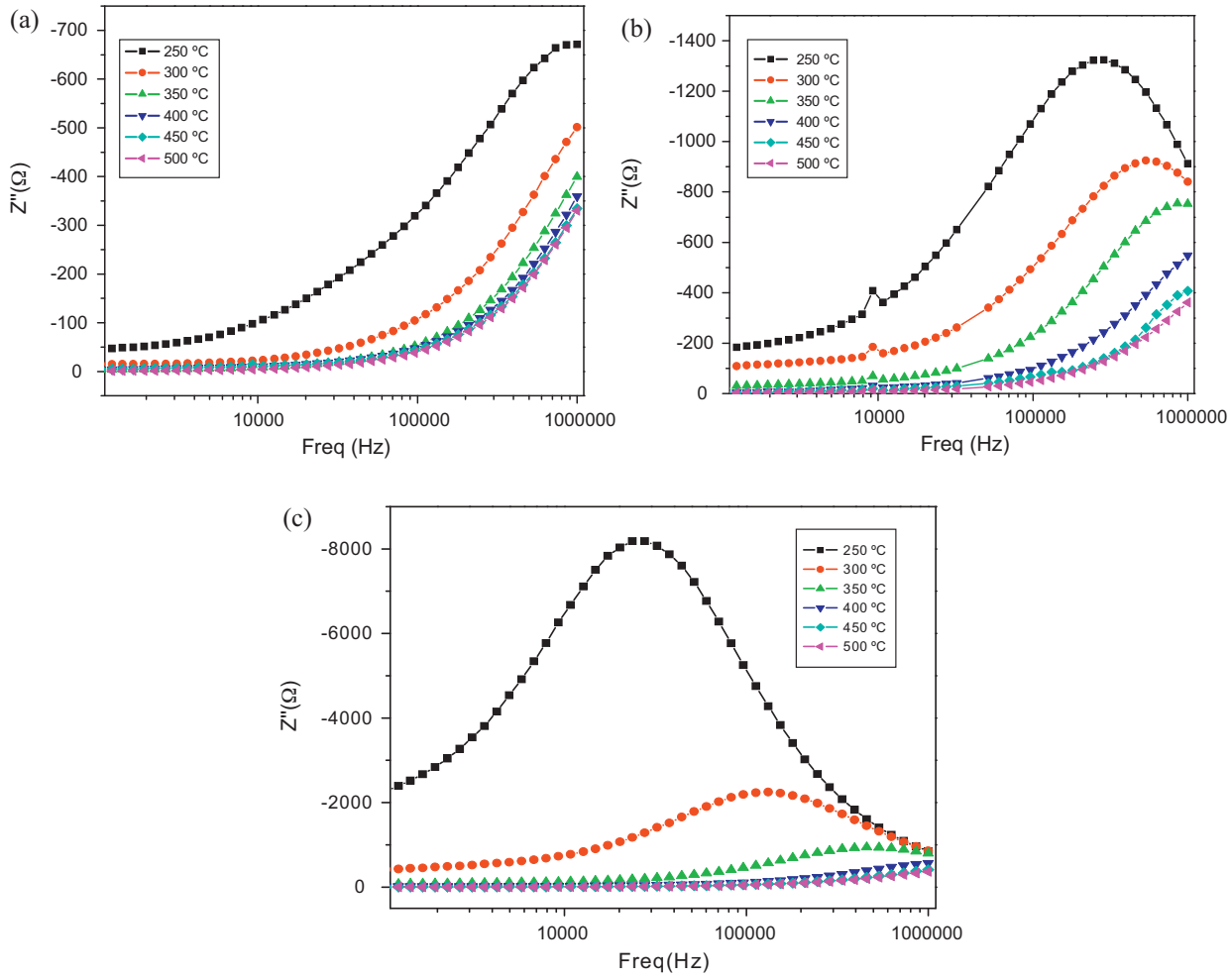

Fig. 6. Frequency variation of imaginary part of impedance of BST–CCF composites with $x = 0.15$, 0.30, 0.45 at different temperature.

polarizations in the material, and the appearance of the peak(s) being a result of dipolar contribution. As the concentration of CCF increases ($x = 0.15$ to 0.30 to 0.45), the pattern of evolution of the imaginary part of impedance spectrum shows a substantial modification in it with the appearance of peaks in the frequency range of present investigation. This result also shows (beyond doubt) a significant effect of CCF substitution on the electrical behavior of BST.

Thermal behavior of σ_{ac} in the material is shown in Fig. 7(a–c). The conductivity increases with increase in temperature. Therefore, BST–CCF exhibits negative temperature coefficient of resistance (NTCR) like semiconductors. The main contribution to the conductivity at high temperature may result from space charge. As temperature increases, space charges are released and recombined and hence curves merge at high temperature. σ_{ac} is strongly related to concentration of mobile ions. Ionic conductivity is mainly dominated by total number of mobile ions and their mobility. On the other hand, it has been reported [28] that the oxygen vacancies exist in single ionized state with activation energy values in the range of 0.3–0.4 eV. For Pb-based perovskite ferroelectrics, activation energies values in the range of 0.6–1.2 eV are commonly associated to doubly-ionized oxygen vacancies. For the BST–CCF composites, a higher activation energy value (1.07 eV) suggests a lower oxygen vacancies concentration, whose values are closer to those values associated to doubly-ionized oxygen vacancy [29]. The released electrons may be captured by Fe^{3+} and generates a reduction of the valence, following the relation.

$$Fe^{3+} + e' \leftrightarrow Fe^{2+}$$

Thus, the conduction process can occur due to the hopping of electrons between Fe^{3+} and Fe^{2+}, leading to the contribution of both single and doubly-ionized oxygen vacancies and the hopping energy between these localized sites for the activation energy in the paraelectric phase region for the studied compositions. The presence of oxygen vacancies would distort the actual ionic dipoles due to the Fe^{3+} ions. The decay of polarizations due to the distorted ionic dipoles could be the cause for the dielectric relaxation processes.

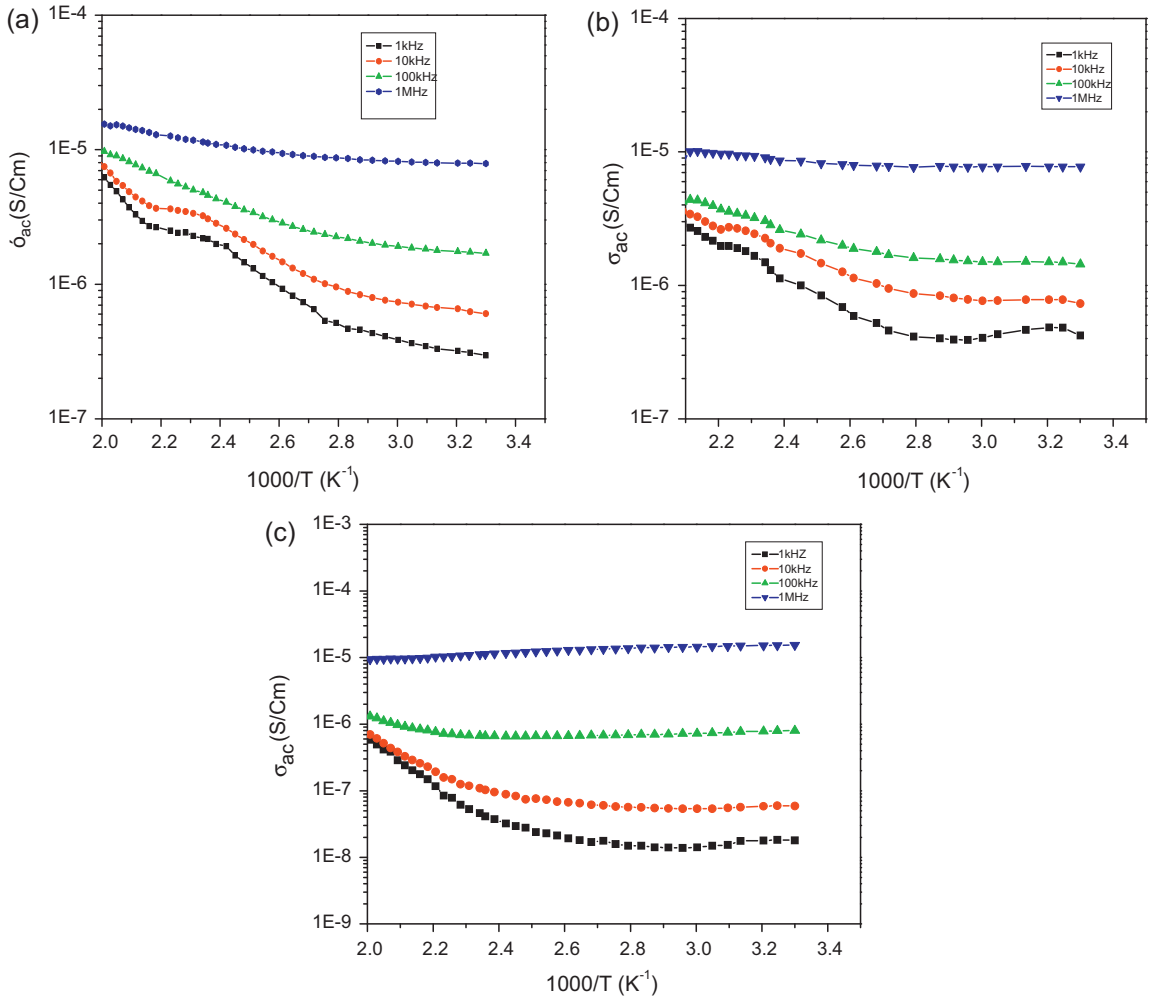

Fig. 7. Temperature dependence of the σ_{ac} of BST–CCF composites with $x = 0.15$, 0.30, 0.45 at different frequency.

5. Conclusion

The present work reports the result of our investigation on the dielectric and electrical properties of BST–CCF composites synthesized by modified wet chemical technique. All the composites show perovskite–spinel crystal structure. The dielectric study of the composites reveals that the effect of ferrite on the ferroelectric component in the composites is to shift the ferroelectric–nonferroelectric transition to the temperature side. The electrical property exhibits that the material exhibits (a) bulk conduction for $x = 0.15$, 0.30, and 0.45 upto 250 °C, (b) grain boundary condition for $x = 0.15$, 0.30 and 0.45 for temperature > 250 °C, (c) negative temperature coefficient of resistance (NTCR) behavior, and (d) temperature dependent relaxation phenomena. The activation energy calculated from the conductivity pattern increases with the increase in ferrite content. This activation energy may be attributed to the oxygen vacancy motion.

Acknowledgment

The author, Kavita Verma, is grateful to Department of Science and Technology, Govt of India for providing financial support under the scheme WOS-A (Ref. No. PS-03-2008).

References

[1] R.T. Hsu, J.H. Jean, Journal of the American Ceramic Society 88 (2005) 2429–2434.
[2] N.A. Hill, Journal of Physical Chemistry 104 (2000) 6694–6709.
[3] Z. Yu, C. Ang, Journal of Materials Science 13 (2002) 193–196.
[4] K. Uchino, Ferroelectric Devices, Dekker, New York, 2000.
[5] J. Zhai, N. Cai, Z. Shi, Y. Lin, C.W. Nan, Journal of Physics D: Applied Physics 37 (2004) 823–827.
[6] J. Ryu, A.V. Carazo, K. Uchino, H.E. Kim Japan, Journal of Applied Physics 40 (2001) 4948–4951.
[7] R.S. Devan, S.A. Lokare, D.R. Patil, Y.D. Kolekar, B.K. Chougule, Journal of Physics and Chemistry of Solids (2006) 1524–1530.
[8] K.K. Patankar, V.L. Mathe, A.N. Patil, S.A. Patil, S.D. Lotake, Y.D. Kolekar, P.B. Joshi, Journal of Electroceramics 6 (2001) 115–122.
[9] M.R. Valenzuela, Magnetic Ceramics, Cambridge University Press, Cambridge, 1994.
[10] L.C. Sengupta, S. Sengupta, IEEE Transactions on Ultrasonics, Ferroelectrics, and Frequency Control 44 (1997) 793–795.
[11] F.A. Miranda, G. Subramanyam, F.W. Van Keuls, R.R. Romanofsky, J.D. Warner, C.H. Mueller, IEEE Transactions on Microwave Theory and Techniques 48 (2000) 1181–1189.
[12] X. Qi, J. Zhou, Z. Yue, Z. Gui, L. Li, Journal of Magnetism and Magnetic Materials 269 (2004) 352–358.
[13] D.J. Bergman, Physics Reports: Physics Letters 43 (1978) 377–407.
[14] D.J. Bergman, Physical Review B 19 (1979) 2359–2368.
[15] C.A. Grimes, D.M. Grimes, Journal of Applied Physics 69 (1991) 6168–6183.

[16] D.C. Sinclair, A.R. West, Journal of Applied Physics 66 (1989) 3850–3856.
[17] A.R. West, D.C. Sinclair, N. Hirose, Journal of Electroceramics 1 (1997) 65–71.
[18] J.R. Macdonald, Impedance Spectroscopy, Emphasizing Solid Materials and Systems, Wiley Interscience Publication, New York, 1987.
[19] J.T.S. Irvine, D.C. Sinclair, A.R. West, Advanced Materials 2 (1990) 132–138.
[20] K. Verma, S. Sharma, Physica Status Solidi B 249 (2012) 209–216.
[21] R. Gerhardt, Journal of Physics and Chemistry of Solids 55 (1994) 1491–1506.
[22] K. Verma, S. Sharma, D.K. Sharma, R. Kumar, R. Rai, Advanced Materials Letters 2 (2011) 163–168.
[23] K. Verma, R. Rai, S. Sharma, Integrated Ferroelectrics 119 (2010) 55–65.
[24] K.K. Patankar, S.S. Joshi, B.K. Chougule, Physics Letters A 346 (2005) 337–341.
[25] L.L. Hench, J.K. West, Principles of Electronics Ceramics, John Wiley and Sons, New York, 1990.
[26] O. Reymond, R. Font, N.S. Almodovac, J. Poetelles, J.M. Siqueiros, Journal of Applied Physics 97 (2005) 108–115.
[27] J.R. Macdonald, Impedance Spectroscopy, Wiley, New York, 1987.
[28] B.S Kang, S.K. Choi, C.H Park, Journal of Applied Physics 94 (2003) 1904–1911.
[29] A. Peláiz-Barranco, Y. González-Abreu, R. López-Noda, Journal of Physics: Condensed Matter 20 (2008) 505208–505213.